**PAPER • OPEN ACCESS**

# Optimization Design and Experimental Study of S-shaped Inlet

To cite this article: Yinhui Shang *et al* 2021 *J. Phys.: Conf. Ser.* **1985** 012001

View the article online for updates and enhancements.

# Optimization Design and Experimental Study of S-shaped Inlet

**Yinhui Shang \*, Changjie Ge, Lianghua Xiao and Jieke Yao**

Chengdu Aircraft Industry (Group) Co., Ltd, Chengdu, China

*Corresponding author e-mail: Yinhui Shang@cac.avic.com

**Abstract.** Lip and diffuser are two important parts of S-shaped inlet, which are difficult to balance in the optimization design of S-shaped inlet. This paper presents an optimization method for S-shaped inlet. Firstly, the parametric models of the lip and the diffuser are established. Combining with automatic mesh generation technology, numerical simulation and genetic algorithm, an optimization platform of s-shaped inlet design based on Isight is established. Aiming at the design of inlet for an unmanned aerial vehicle (UAV), compared with the prototype, the total pressure recovery coefficient of the optimized inlet obtained by this optimization method is increased by 1.5%, and the steady-state circumferential distortion is reduced by 58.6%. The wind tunnel experiment is carried out to obtain the aerodynamic performance of the inlet, and the experimental results are in good agreement with the numerical simulation results.

## 1. Introduction

S-shaped inlet has been widely used in UAV and all-wing aircraft due to its advantages of stealth, reduction of drag and improvement of lift [1-3]. Area expansion of the S-shaped inlet will lead to the adverse pressure gradient from entrance to exit, while the wall curvature will lead to the adverse pressure gradient at the local wall [4]. Thus, the problem of flow separation may exist and lead to the low total pressure recovery coefficient of the inlet and large distortion at the outlet. In recent years, the optimization design of S-shaped inlet combined with CFD has received more and more attention.

A lot of research has been done on the design and optimization of S-shaped inlet. Rodriguez [5, 6] and others carried out the multi-objective optimization design of BLI inlet, taking the attack angle, back pressure at outlet, lip profile as optimization variables, taking the total pressure recovery coefficient, total pressure distortion coefficient, lift coefficient, drag coefficient and fuel consumption rate as the optimization objectives, iterating through the optimization algorithm based on pressure gradient to obtain the optimal inlet geometry. In 2005, Lee et al. [7] used the adjoint matrix method to optimize the design of the S-shaped inlet, and many design parameters were expressed by the adjoint matrix. Knight et al. [8] developed a new method to integrate the most advanced CFD analysis, combining the non-uniform rational B-spline technique with optimization theory to design and optimize the three-dimensional S-shaped inlet, and this method can be automatically re-designed. In 2008, Zhang et al. [9] used Hicks Henne function as the basis function to construct the centerline and cross-sectional area, and used Carbide orthogonal decomposition (POD) to generate the optimal solution under the least square method. After optimization, the aerodynamic performance of the inlet was significantly improved.

Lefantzi [10] studied the optimization design of subsonic inlet with total pressure distortion as the optimization objective. Hyo [11] proposed a global optimization method based on Kriging model.

The lip and diffuser have an important influence on the performance of the inlet, which are usually designed and studied respectively. In this paper, Matlab is used to carry out the parametric modeling of the inlet lip and diffuser at the same time. Some key parameters in the design of the lip and diffuser are selected as the variables of the optimization design. These parameters are introduced into the modeling. Based on the completion of the parametric modeling, Isight is used as the platform to integrate MATLAB, ICEM and CFX for the optimization design of the s-shaped inlet. The flow field and inlet performance quality before and after optimization are compared. Results show that the inlet performance is obviously improved after optimization. Finally, the performance of the inlet under different working conditions is obtained through wind tunnel test, and the results are compared with CFD calculation.

## 2. Optimal design of S-shaped inlet

### 2.1. Prototype of the inlet

In this paper, the inlet is arranged on the back of the UAV, and there is a long fuselage in front of the inlet, so the boundary layer is set to eliminate the low energy flow. Fig. 1 shows the three-dimensional model of UAV without wing, Fig. 2 shows the front view and axonometric view of the prototype with fuselage. The green part is the lip, and the lip profile is a semicircle with a radius of 6 mm. The red part is the inlet diffuser, which is obtained through the multi-section surface command in CATIA. The inlet is meshed and numerically calculated in order to investigate its performance. Fig. 3 shows the side view of inlet with CFD extension.
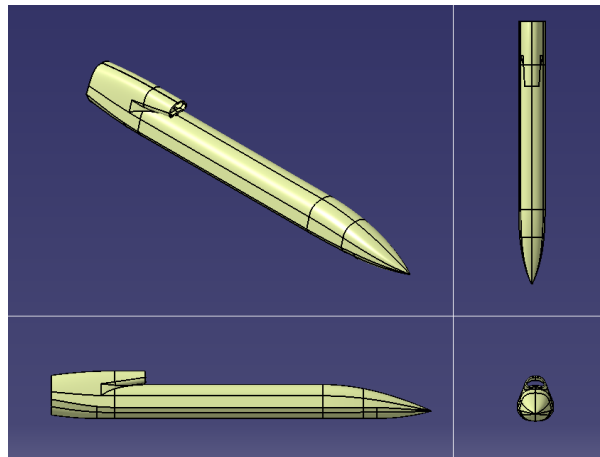


**Figure 1.** Three-dimensional model of UAV without wing.



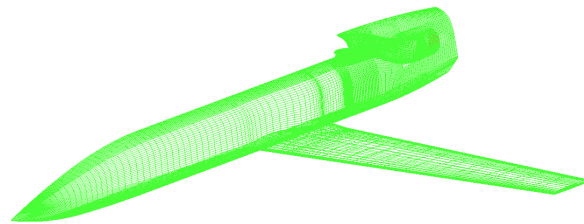**Figure 2.** Front view and axonometric view of the prototype with fuselage.
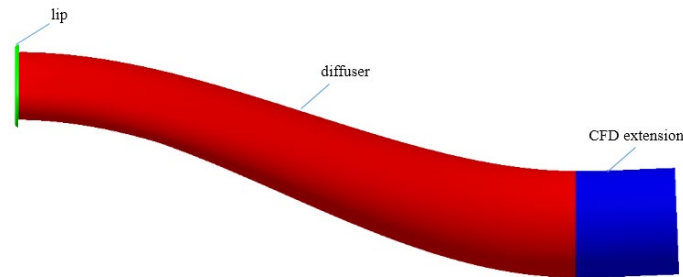
**Figure 3.** Side view of inlet with CFD extension

ICEM is used to generate structured grid. Because of the symmetry of the inlet, the half model can be used when there is no side slip angle. The number of grid cells is about 4.02 million. Fig. 4 shows the grid of flow field, and Fig. 5 shows the surface mesh of the inlet model.

In this paper, the standard SST turbulence model is used in the numerical simulation. The convergence criterion is that the residuals are reduced to four orders of magnitude and the flow at the exit section of the inlet is stable.
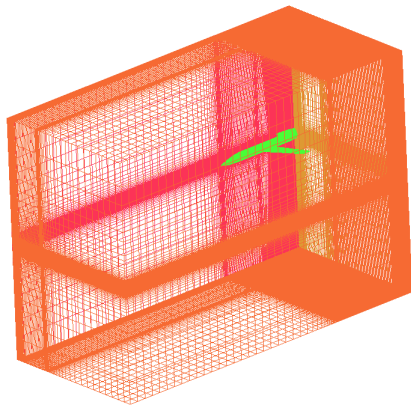


**Figure 4.** Grid of flow field.          **Figure 5.** Surface mesh of the inlet model.

The numerical simulation of the inlet in different working conditions is carried out. The results show that the performance of the inlet is extremely bad when free stream Mach number is zero (Ma0=0). Fig. 6 shows the total pressure recovery coefficient at symmetry plane and outlet, it can be seen that there is a serious total pressure loss at the bottom of the inlet. The total pressure recovery coefficient $\sigma$ is 0.936 and the steady-state circumferential distortion $\Delta\overline{\sigma}_0$ is 0.075. The comprehensive distortion of the engine is required to be less than 8%. The combined distortion of this inlet can easily exceed 8% under the condition of steady distortion and dynamic distortion, so it is necessary to optimize the inlet to meet the safety requirements.
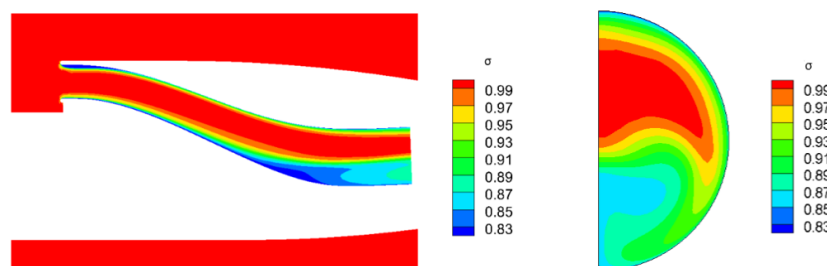


**Figure 6.** Total pressure recovery coefficient at symmetry plane and outlet of the prototype.

### 2.2. Optimization design scheme

*2.2.1. Overall idea of optimization design.* Optimization design refers to the selection of the best scheme from a variety of schemes. The basis of optimization is the mathematical optimization theory. The process of optimization design generally includes giving optimization variables, setting objective function, and using computer tools to select the optimal scheme from multiple schemes satisfying constraint conditions. For the optimization design of the inlet combined with CFD, the parametric model of the inlet can be established, and then it can be meshed and numerically calculated to evaluate the performance of the inlet. The optimal inlet model can be obtained by optimizing the control parameters of the inlet through a certain algorithm. According to this optimization idea, an optimization platform can be built to realize the optimization process. The flow chart of the whole optimization design scheme is shown in Fig. 7.
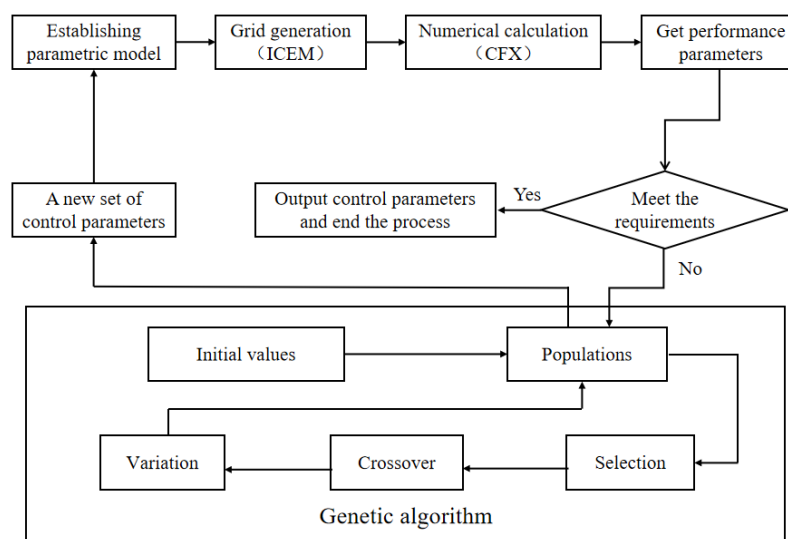


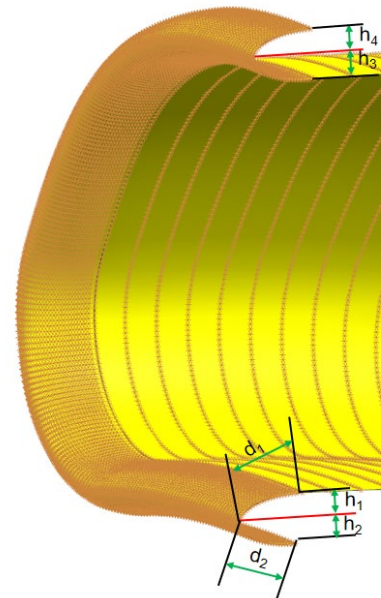**Figure 7.** Flow chart of the whole optimization design scheme.

*2.2.2. Parametric modeling of lip.* In order to facilitate parametric modeling, quarter ellipse is selected to represent the shape of the inner lip and the outer lip. Because of the symmetry of the inlet, a half model is established. The leading edge of lip is shown in Fig. 8, and it is discretized into 101 points as shown in Fig. 9. The point at the bottom of the inlet is taken as the starting point, and the point at the top of the inlet is taken as the ending point. Each point is taken as the vertex of the quarter ellipse. The inner lip and the outer lip are composed of 101 quarter ellipses. Among the 101 quarter-ellipse lines forming the inner lip, the thickness of the quarter-ellipse corresponding to the starting point is the starting thickness of the inner lip, denoted as h1, and the thickness of the quarter-ellipse corresponding to the ending point is the ending thickness of the inner lip, denoted as h3. Among the 101 quarter-ellipse lines forming the outer lip, the thickness of the quarter-ellipse corresponding to the starting point is the starting thickness of the outer lip, denoted as h2, and the thickness of the quarter-ellipse corresponding to the ending point is the ending thickness of the outer lip, denoted as h4. The thicknesses of the 101 quarter ellipses that forming the inner lip and the outer lip vary uniformly from the starting thickness to the ending thickness. Denote the length of the inner lip as d1 and the length of the outer lip as d2. Fig. 10 shows the geometric parameters of lip. In order to reduce the design variables, the length d1=d2=d. The low pressure region mainly exists at the bottom of the inlet, so we focus on optimizing the shape of the lower lip. Make the thickness of the upper lip the same as that of the prototype, that is, h3=h4=6mm. Therefore, there are three variables: h1, h2 and d. The range of variables h1, h2 and d in optimization design is shown in Table 1.
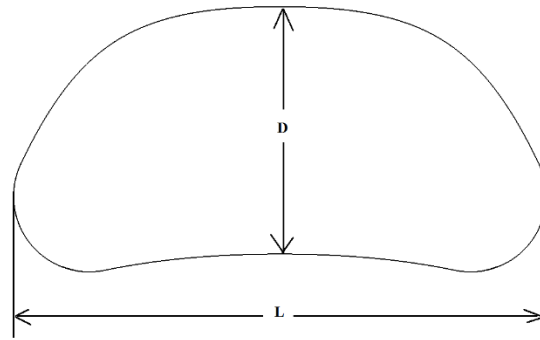
**Figure 8.** Shape of lip leading edge
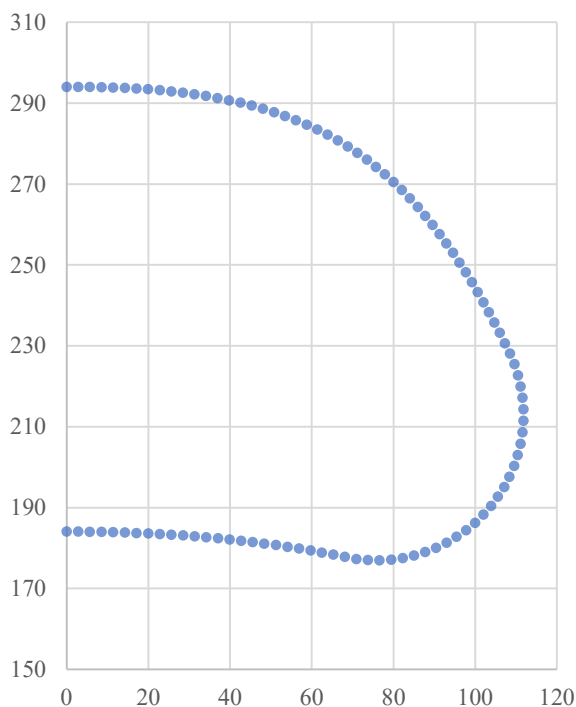


**Figure 9.** Discrete points of lip leading edge.    **Figure 10.** Geometric parameters of lip.

**Table 1.** The range of variables h1, h2 and d in optimization design.

| Parameters | Minimum | Maximum |
|:---:|:---:|:---:|
| $h_1$ | 4 | 15 |
| $h_2$ | 4 | 15 |
| d | 4 | 20 |

*2.2.3. Parametric modeling of diffuser.* After completing the parameterized modeling of lip, the throat points coordinate can be obtained as the entrance of the diffuser, which are 101 discrete points. The exit can also be divided into 101 discrete points. There are several sections from entrance to exit, and each section is composed of 101 points. If the shapes of entrance and exit are determined, the curvature can be calculated. Set the curvature distribution from entrance to exit, the curvature of all sections along the s-shaped inlet can be obtained. Given centerline distributions and area distributions, the coordinates of all points are obtained through mathematical solution and coordinate transformation, and the diffuser modeling is completed. The distributions of centerline and area from entrance to exit are the key

parameters that affect the performance of S-shaped inlet. We use the quartic polynomial to express the distributions, which is expressed as equation (1).

$$y = ax^2 + bx^3 + cx^4 \tag{1}$$

The coefficient a, b and c in the equation have the restricted condition as shown in equation (2). It can be seen that there are 2 valid equations with 3 unknowns in equation (1). As a result, the equation has one degree of freedom to adjust the shape of the graph.

$$\left. \begin{array}{l} y|_{x=1} = 1 \rightarrow a + b + c = 1 \\ \frac{dy}{dx}|_{x=1} = 0 \rightarrow 2a + 3b + 4c = 0 \end{array} \right\} \tag{2}$$

In this paper, the value of a is discussed. Given a value of a, the values of b and c can be obtained, and the quartic polynomial curve is determined.

There are three analytical functions to represent the centerline shape and area distribution, which are shown in equations (3), (4) and (5). Equations (3) represents rapid turning at the exit. Equations (4) represents modest turning from entrance to exit. Equations (5) represent rapid turning at the entrance. For equation (1), when a = 0, it can be calculated that b = 4, c = - 3, and then equation (1) is equivalent to equation (3). When a = 3, it can be calculated that b = -2, c = 0, and then equation (1) is equivalent to equation (4). When a =6, it can be calculated that b =-8, c =3, and then equation (1) is equivalent to equation (5).

$$y = 4x^3 - 3x^4 \tag{3}$$

$$y = 3x^2 - 2x^3 \tag{4}$$

$$y = 6x^2 - 8x^3 + 3x^4 \tag{5}$$

Fig. 11 shows the diagram of quartic polynomial curves with different values of 'a'. It can be seen that the larger a is, the rapider turning the curve has at the first half. Fig. 12 shows the diffuser represented by points. For the design of the diffuser, the quadratic coefficient of the quartic polynomial representing centerline distribution is a1, and the quadratic coefficient of the quartic polynomial representing area distribution is a2. In this paper, a1 and a2 can be used as the control parameters of the diffuser modeling.The range of variables a1 and a2 in optimization design is shown in Table 2.
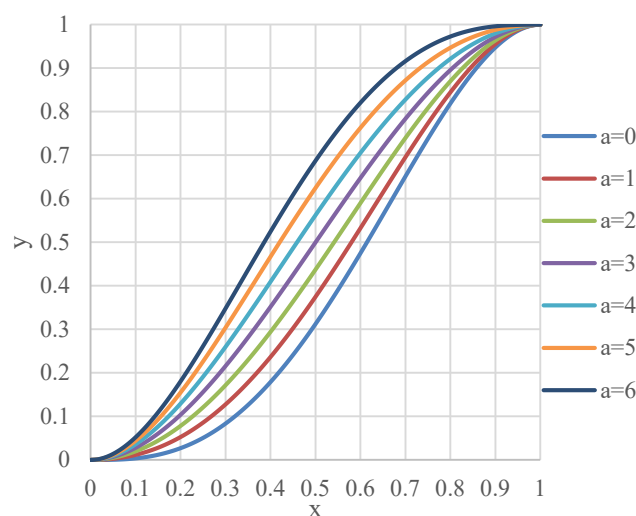


**Figure 11.** Diagram of quartic polynomial curve with different values of 'a'.
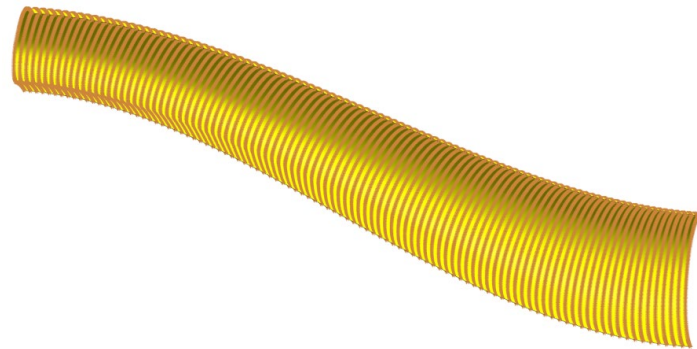
**Figure 12.** The diffuser represented by points.

**Table 2.** Range of variables a1 and a2.

| Parameters | Minimum | Maximum |
|---|---|---|
| $a_1$ | -2 | 8 |
| $a_2$ | -2 | 8 |

*2.2.4.  Automatic meshing.* In order to realize the whole optimization process, it is necessary to conduct automatic mesh generation for each inlet model. In order to improve the calculation speed, the inlet model is not equipped with fuselage and wing. The command stream of ICEM is used for automatic mesh generation. Importing the parametric model of the s-shaped inlet into ICEM in the form of points and lines, and then we can call the command stream to quickly generate and output the mesh. Fig. 13 shows the grid generated with the command stream.
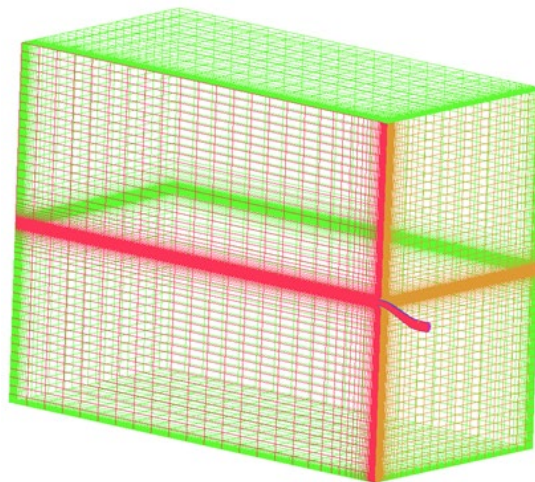


**Figure 13.** Grid generated with the command stream.

*2.3.  Optimization platform*

According to the optimization design scheme shown in Fig. 7, the optimization platform is built as shown in Fig. 14. Firstly, using Matlab to generate geometric data and import the geometric data into ICEM to generate the grid. Then, setting the boundary conditions by using the 'cfxpre' component and do numerical calculation by using the 'cfxsolve' component. Finally, the 'cfxpost' component is used to evaluate the performance of the inlet. Taking total pressure recovery coefficient and steady-state circumferential distortion as the optimization objectives. If the aerodynamic performance is optimal, the control parameters will be output and the optimization process is end, otherwise, a new set of optimization variables will be given according to the optimization algorithm and the next round of optimization will begin.
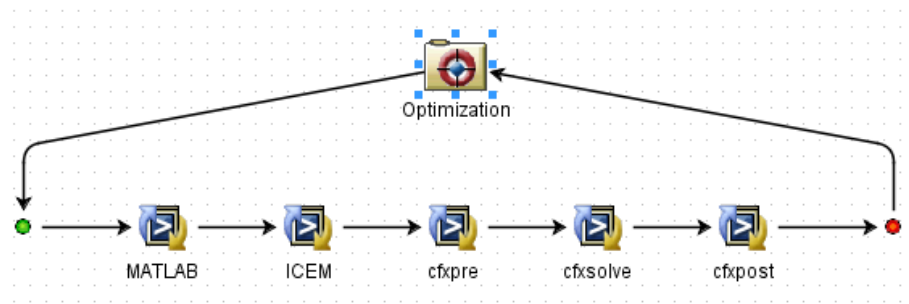
**Figure 14.** Optimization platform based on Isight.

### 2.4. *Optimization Results*

After several rounds of iteration, control parameters after optimization are shown in Table 3. The two-dimensional profiles at symmetry plane of the optimized model and the prototype are shown in Fig. 15, and the lip profiles of the optimized model the prototype are shown in Fig. 16.

It can be seen that the centerline distribution of the optimized model is rapider than that of the prototype. After optimization, the lower lip is thicker, which can improve the flow field quality near the lower lip.

**Table 3.** Control parameters after optimization.

| Parameters | $h_1$ | $h_2$ | d | $a_1$ | $a_2$ |
|---|---|---|---|---|---|
| Optimization value | 10.2 | 8.4 | 14.8 | 4.7 | 3.5 |
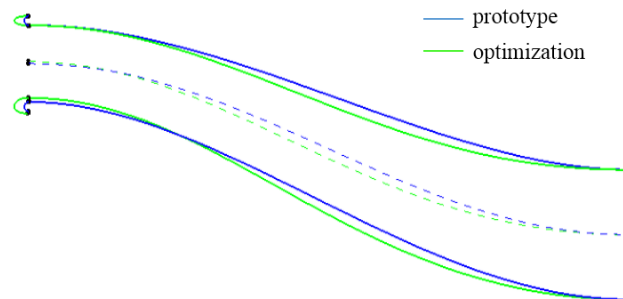


**Figure 15.** Two-dimensional profiles at the symmetry plane of the optimized inlet and the prototype.
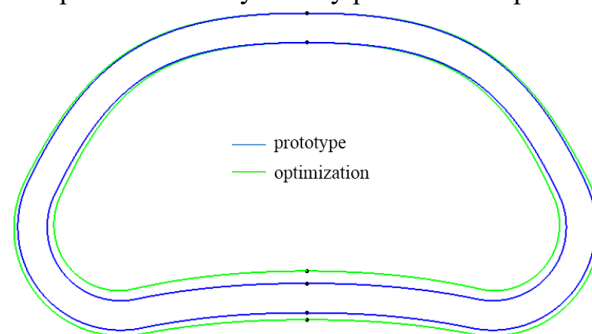


**Figure 16.** Lip profiles of the optimized model the prototype.

Fig.17 shows the total pressure recovery contour of prototype at the symmetry plane when Ma0=0, and Fig. 18 shows that of the optimized model. It can be seen that the total pressure recovery coefficient of prototype is lower at the lower wall of the inlet, which will bring a larger total pressure loss. Fig. 19 shows the streamlines near the lip of prototype, and Fig. 20 shows the streamlines near the lip of the optimized model. It can be seen that the flow separation occurs at the upper lip of the two kinds of inlets,
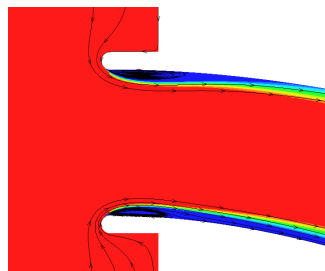
and the flow separation also occurs at the lower lip of the prototype, which will inevitably bring about the loss of total pressure.
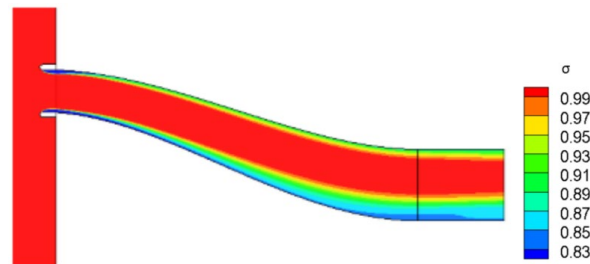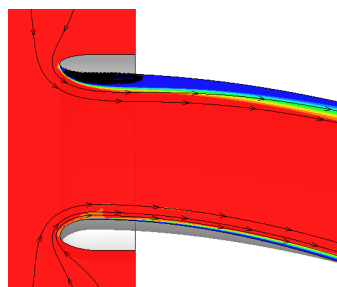


**Figure 17.** Total pressure recovery contour of prototype at the symmetry plane when Ma0=0.
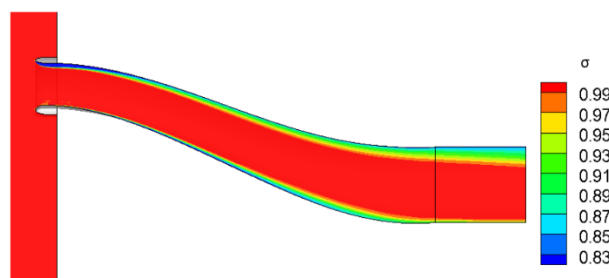


**Figure 18.** Total pressure recovery contour of the optimized model at the symmetry plane when Ma0=0.



**Figure 19.** Streamlines near the lip of prototype.



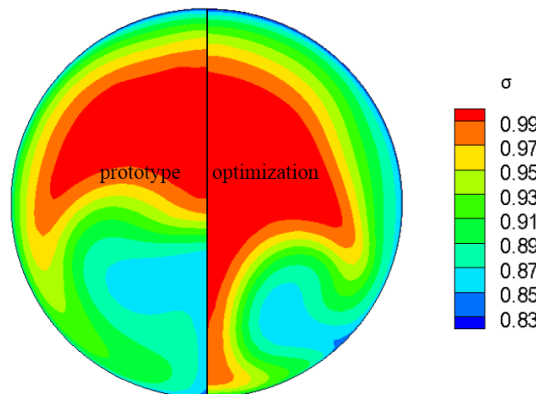**Figure 20.** Streamlines near the lip of the optimized model.

Fig. 21 shows the total pressure recovery contour of prototype and the optimized model at the exit without fuselage and wing. It can be seen that the total pressure recovery coefficient at the bottom of the inlet of the optimized model is significantly higher than that of the prototype. The low total pressure zone of the prototype is distributed at the bottom of the whole exit, while the low total pressure zone of the optimized model distributed on both sides of the bottom. Obviously, the total pressure distribution

after optimization is more uniform, so the steady-state circumferential distortion will be significantly lower than prototype.
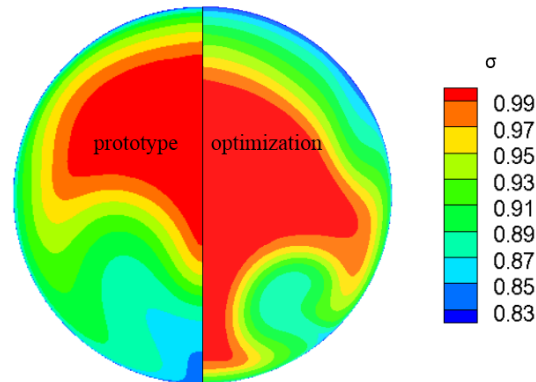


**Figure 21.** Total pressure recovery contour of prototype and the optimized model at the exit without fuselage and wing.

The numerical simulation of the optimized inlet with fuselage and wing is carried out. Fig. 22 shows the total pressure recovery contour of prototype and the optimized model with fuselage and wing. Comparing with Fig. 21, the total pressure recovery contour of the inlet with fuselage and wing is similar to that without fuselage wing. Table 4 shows the performance of prototype and the optimized model. It can be seen that the total pressure recovery coefficient of the optimized model is higher and the steady-state circumferential distortion is lower. The total pressure recovery coefficient of the optimized model is increased by 1.5%, and the steady-state circumferential distortion is reduced by 58.6% compared with prototype.



**Figure 22.** Total pressure recovery contour of prototype and the optimized model at the exit with fuselage and wing.

**Table 4.** Performance of prototype and the optimized model.

| Inlet model | $\sigma$ | $\Delta\overline{\sigma}_0$ |
|---|---|---|
| Prototype | 0.936 | 0.075 |
| Optimized model | 0.950 | 0.031 |

## 3. Experiment and discussion

The low speed wind tunnel experiment was carried out in Shenyang Aerodynamics Research Institute. The experimental model scale is 2.5. The experimental model is shown in Fig. 23, and the s-shaped inlet model installed in the wind tunnel is shown in Fig. 24. During the experiment, the angles of attack vary from -3° to 15° , the Side-Slip angles from 0° to 6° and the free stream Mach number from 0 to 0.2.
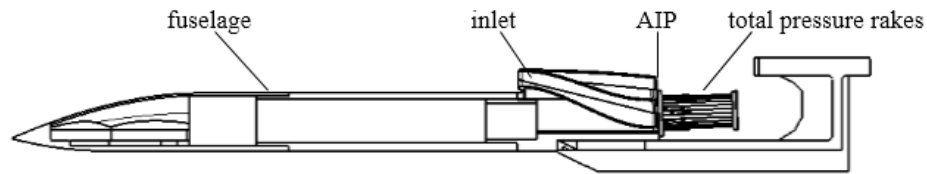
**Figure 23.** Experimental model.
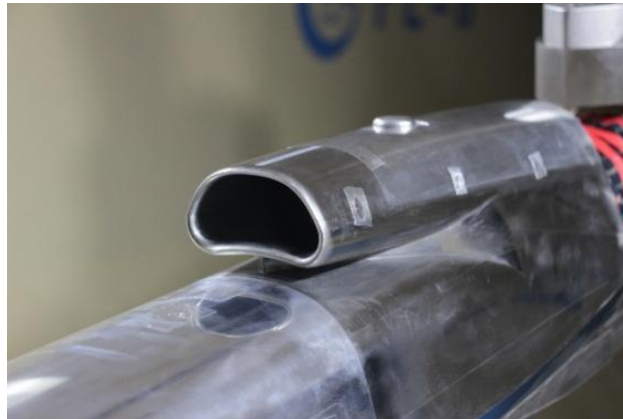


**Figure 24.** S-shaped inlet model installed in the wind tunnel.

### 3.1. Effects of free stream Mach number $Ma_0$

Fig. 25 and fig. 26 show the effect of free stream Mach number $Ma0$ on the total pressure recovery $\sigma$ and the steady-state circumferential distortion index $\Delta\overline{\sigma_0}$ at the exit. With the increasing of $Ma0$, the total pressure recovery coefficient increases and the steady-state circumferential distortion decreases.
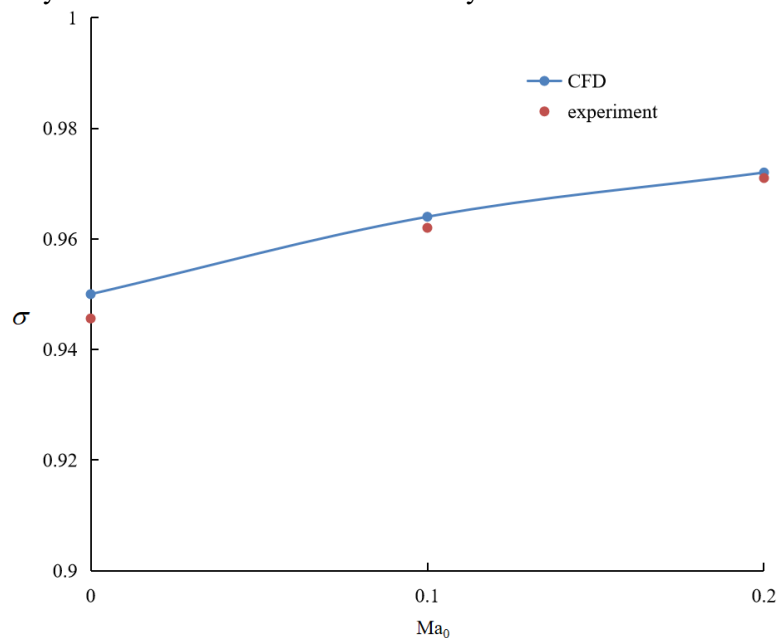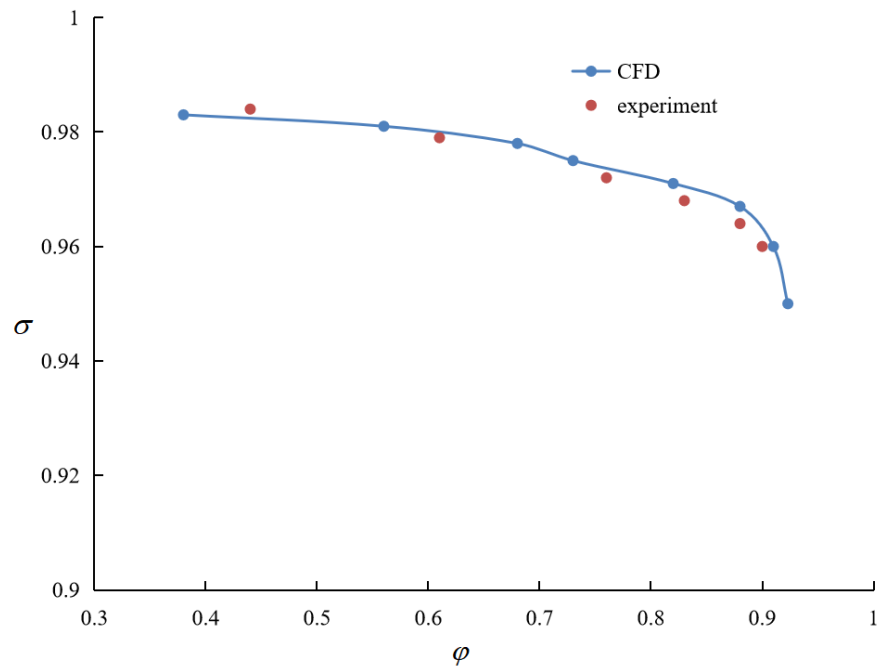


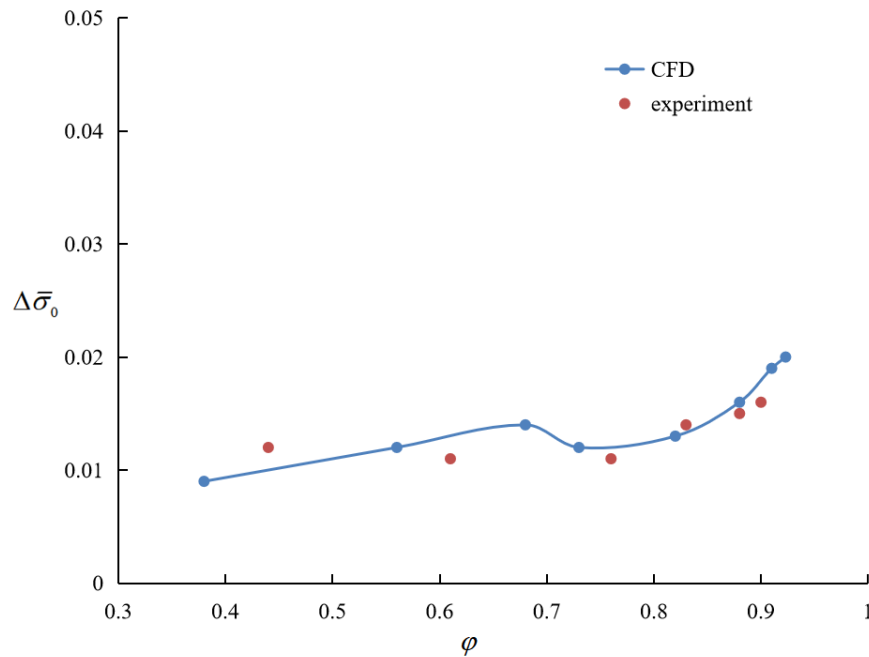**Figure 25.** Total pressure recovery versus free stream Mach number.
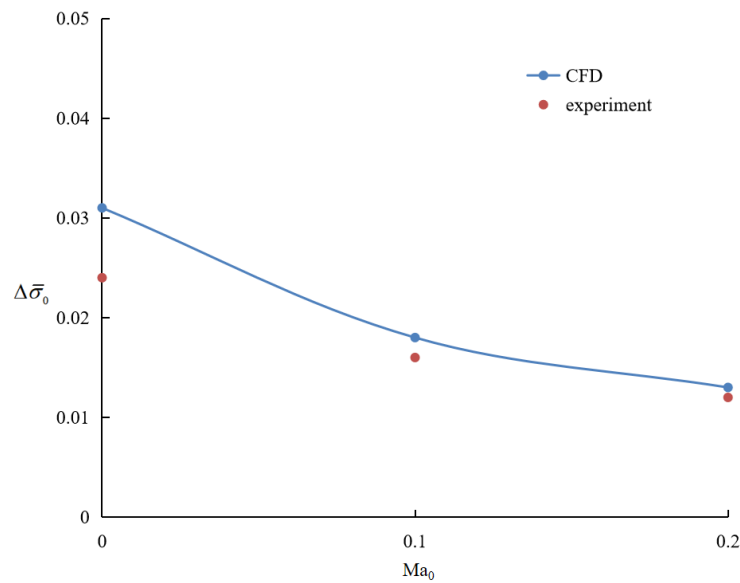
**Figure 26.** Steady-state circumferential distortion versus free stream Mach number.

### 3.2. Effects of mass flow ratio

Fig. 27 and fig. 28 show the variation of total pressure recovery coefficient and steady-state circumferential distortion with mass flow ratio when free stream Mach number $Ma0 = 0.2$, attack angle $\alpha=0$ and sideslip angle $\beta=0$. It can be seen that the CFD values are in good agreement with the experimental values. With the increasing of mass flow ratio, the total pressure recovery coefficient shows a downward trend. When the mass flow ratio is greater than 0.85, the total pressure recovery coefficient decreases rapidly. With the increase of mass flow ratio, the steady-state circumferential distortion shows an increasing trend.
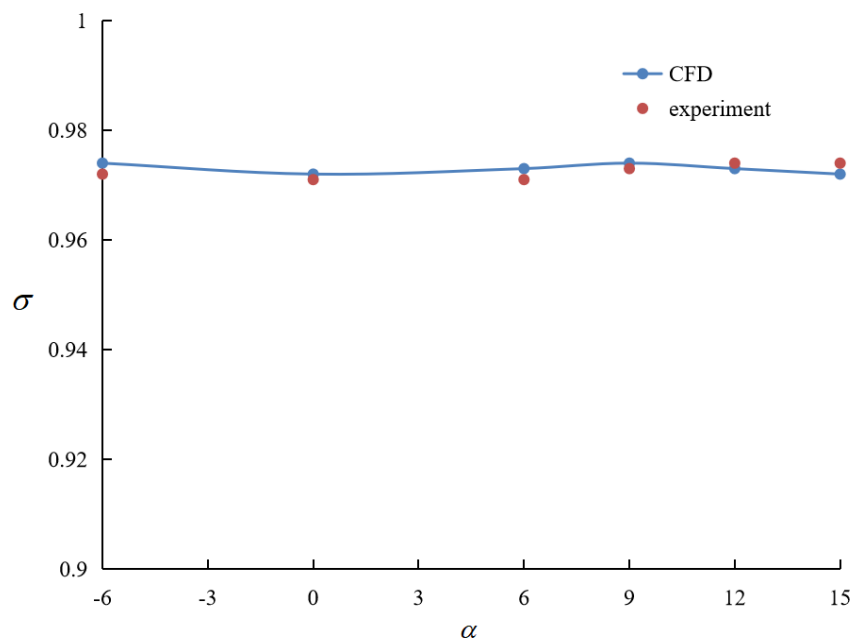


**Figure 27.** Total pressure recovery versus mass flow ratio.

**Figure 28.** Steady-state circumferential distortion versus mass flow ratio.
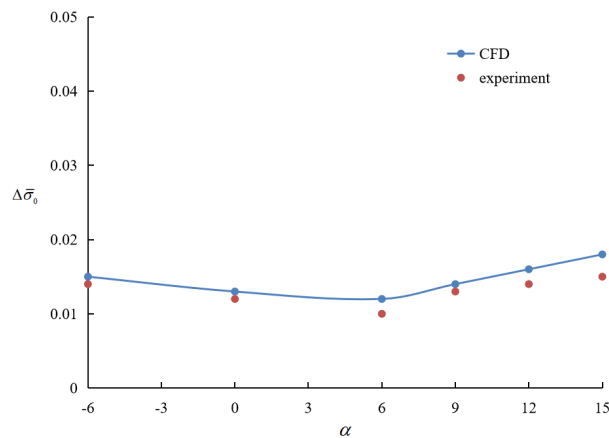
### 3.3. Effects of attack angle

Fig. 29 and fig. 30 show the variation of total pressure recovery coefficient and steady-state circumferential distortion index with attack angle (Ma0=0.2, β=0). Total pressure recovery coefficient changes little with attack angle, and steady-state circumferential distortion increases after an initial decrease. Fig. 31 shows the total pressure recovery contours of the exit obtained from the experiment at different attack angles. It can be seen that with the increase of attack angle, the high total pressure region moves to the bottom of exit.
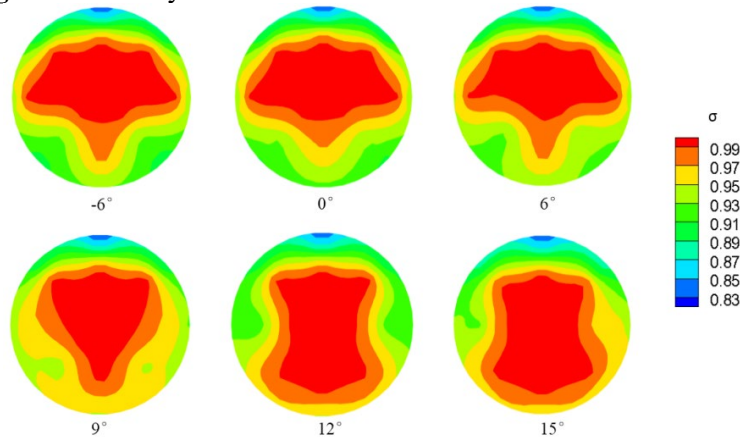


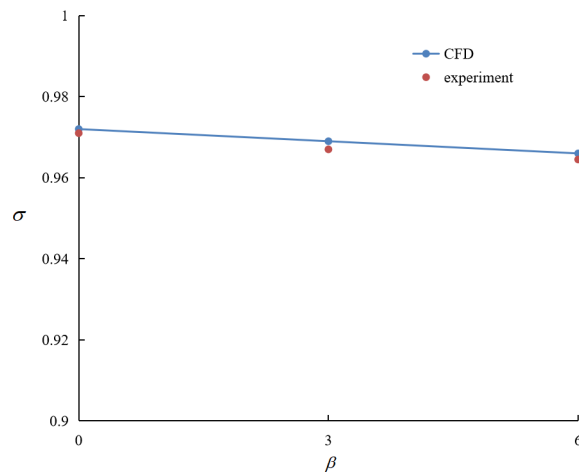**Figure 29.** Total pressure recovery versus attack angle.

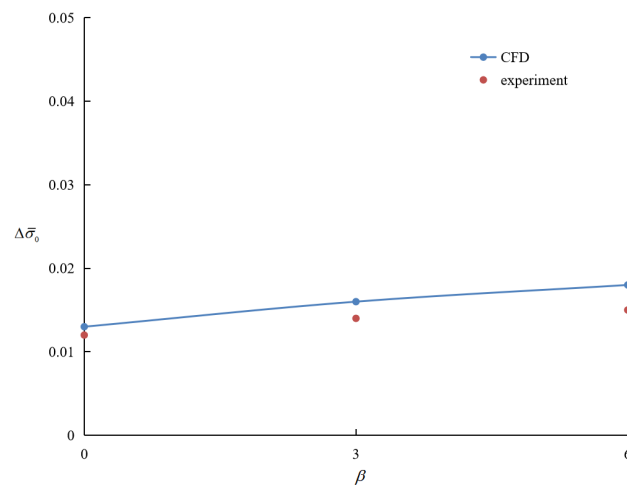**Figure 30.** Steady-state circumferential distortion versus attack angle.



**Figure 31.** Total pressure recovery contours of the exit obtained from the experiment at different attack angles.

### 3.4. Effects of attack angle

Fig. 32 and Fig. 33 show the variation of total pressure recovery coefficient and steady-state circumferential distortion index with sideslip angle. It can be seen that with the increase of sideslip angle, the total pressure recovery coefficient decreases, while the steady-state circumferential distortion increases obviously.



**Figure 32.** Total pressure recovery versus sideslip angle.

**Figure 33.** Steady-state circumferential distortion versus sideslip angle.

## 4. Conclusion

In this paper, an optimization method for S-shaped inlet is proposed. The initial thickness of the inner lip, the initial thickness of the outer lip, the length of the lip, the quadratic coefficient of the quartic polynomial representing the distribution of the centerline, the quadratic coefficient of the quartic polynomial representing the distribution of the area are taken as variables to carry out parameterized modeling. Matlab, ICEM, CFX and other software are integrated into Isight to establish the optimization platform. Aiming at the design of inlet for an, the total pressure recovery coefficient of the optimized model is improved and the steady-state circumferential distortion index is reduced when $Ma0 = 0$ compared with the prototype. Finally, the performance of the inlet is verified by experiment. The CFD calculation results are in good agreement with the experimental results.

## References

[1]    Smith A M O. The Jet Airplane Utilizing Boundary Layer Air for Propulsion [J]. Journal of the Aerona- utical Sciences, 2012, 14(2).

[2]    Smith L H. Wake Ingestion Propulsion Benefit [J]. Journal of Propulsion and Power, 1993, 9(1): 74-82.

[3]    Plas A P, Sargeant M A, Madani V, et al. Performance of a Boundary Layer Ingesting (BLI) Propulsion System[J]. AIAA, 2007, 450:2007.

[4]    Anthony M. Ferrar, Walter F. O'Brien, Progress in Boundary Layer Ingesting Embedded Engine Research [R], AIAA 2012-4283.

[5]    Rodriguez D L. A 3D Multidisciplinary Design Method for Boundary Layer Ingesting Inlets [C]. 38th Aerospace Sciences Meeting and Exhibit. Reno, NV. AIAA-2000-0424.

[6]    Rodriguez D L. Multidisciplinary Optimization Method for Designing Boundary Layer Ingesting Inlets [J]. Journal of Aircraft. 2009, 46(3): 883-894.

[7]    Lee B J, Liou M S, Kim C. Adjoint Based Design Approach for Boundary Layer Ingestion Offset Intake [C]. 19th AIAA Computational Fluid Dynamics. San Antonio, Texas. AIAA 2009-3804.

[8]    Zhang W L, Knight D D, Smith D. Automated Design of a Three- Dimensional Subsonic Diffuser [J]. Journal of Propulsion and Power, 2000, 16(6): 1132-1140.

[9]    Zhang J M, Wang C F, Lum K Y. Multidisciplinary Design of S -shaped Intake [C]. 26th AIAA Applied Aerodynamics Conference. Honolulu, Hawaii. AIAA 2008-7060.

[10]   Lefantzi S, Knight D D. Automated Design Optimization of a Three-Dimensional S-shaped Subsonic Diffuser [J]. Journal of Propulsion &Power, 2002, 18(4): 913-921.

[11]   Hyo G, Bae, Hyung S, et al. Efficient Global Optimization for S-duct Diffuser Shape Design [J]. Proceedings of Institution of Mechanical Engineers, Part G: Journal of Aerospace Engineering, 2013, 227(9): 1516-1532.